Integrated silicon photonic device design by attractor selection mechanism based on artificial neural networks: optical coupler and asymmetric light transmitter

Emre Bor,[1,2] Onur Alparslan,[3] Mirbek Turduev,[2,*] Y. Sinan Hanay,[4] Hamza Kurt,[1] Shin'ichi Arakawa,[3] and Masayuki Murata[3]

[1]Department of Electrical and Electronics Engineering, TOBB University of Economics and Technology, Ankara 06560, Turkey
[2]Department of Electrical and Electronics Engineering, TED University, Ankara 06420, Turkey
[3]Graduate School of Information Science and Technology, Osaka University, Osaka 565-0871, Japan
[4]Department of Computer Engineering, Erzurum Technical University, Erzurum 25700, Turkey
*mirbek.turduev@tedu.edu.tr

Abstract: Recently, different nanophotonic computational design methods based on optimization algorithms have been proposed which revolutionized the conventional design techniques of photonic integrated devices. The intelligently designed photonic devices have small footprints and high operating performance along with their fabrication feasibility. In this study, we introduce a new approach based on attractor selection algorithm to design photonic integrated devices. In order to demonstrate the potential of the proposed approach, we designed two structures: an optical coupler and an asymmetric light transmitter. The designed photonic devices operate at telecom wavelengths and have compact dimensions. The designed optical coupler has a footprint of only 4×2 μm^2 and coupling efficiency of 87.5% at a design wavelength of 1550 nm with spatial beam width compression ratio of 10:1. Moreover, the designed optical coupler operates at a wide bandwidth of 6.45% where the transmission efficiency is above 80%. In addition, the designed asymmetric light transmitter with a size of 2×2 μm^2 has the forward and backward transmission efficiencies of 88.1% and 8.6%, respectively. The bandwidth of 3.47% was calculated for the designed asymmetric light transmitter where the forward transmission efficiency is higher than 80% and the backward efficiency transmission is under 10%. In order to evaluate the operating performance of the designed photonic devices, coupling losses are analyzed. The presented results show that the attractor selection algorithm, which is based on artificial neural networks, can bring a conceptual breakthrough for the design of efficient integrated nanophotonic devices.

1. Introduction

Photonic integrated circuits (PICs) have many advantages over integrated electronic circuits such as having a large bandwidth, resistance to interference and nonexistence of Joule effect [1,2]. On the other hand, PICs have a considerable disadvantage in terms of lower integration density comparing with conventional integrated electronic circuits. In order to overcome the density problem, the silicon-on-insulator (SOI) platforms are introduced, which enable the fabrication of higher integration density for PICs with low power consumption and high efficiency [1,3–5]. Moreover, SOI technology is compatible with complementary metal-oxide-semiconductor (CMOS) fabrication process. Due to high refractive index contrast between silicon (Si) and silicon dioxide (SiO_2), SOI materials are suitable for designing photonic integrated devices (PIDs). In general, design of PIDs depends on theoretical knowledge and educated guess where the design parameters are subjected to brute-force adjustments. However, brute-force tuning approach is not sufficient in the cases where the

problem is to design compact and efficient PIDs. In recent years, diverse approaches are proposed to reduce the footprints and increase the performance of PIDs in the applications of nanophotonics. Recently, the use of optimization algorithms enabled the design of compact and high efficiency PIDs. For this purpose, the inverse design method was developed to design several nanophotonic devices such as mode converters, fiber couplers, and wavelength demultiplexers [6–8]. Also, nonlinear search algorithm was applied to design a polarization beam splitter and optical diodes [9,10]. Recently, a machine learning algorithm was introduced to design a subwavelength focusing lens and an optical coupler [11]. Moreover, a tandem of deep neural networks was utilized to predict the geometry of a structure for a desired response which still suffers from requiring a large data set [12]. These studies indicate that the future of PICs/PIDs will heavily depend on automated intelligent design approaches [13].

In general, the efficient transmission of light between PIDs is an essential characteristic for the performance of PICs. Here, it is important to provide a sufficient amount of injected optical power to the PICs from the free-space because the injected light that circulates within the PICs effects the proper operation of PIDs. However, coupling of light from free-space to PIDs through the optical waveguides is a challenging issue in SOI platforms due to high refractive index contrast and difference of mode orders between optical fibers and waveguides. For this reason, design of an optical coupler that confines the incident light into a waveguide is important for applications of PICs. In this regard, various methods have been introduced to couple incident light into a waveguide with high coupling efficiency and large bandwidth, and to reduce the dimensions of optical couplers [11,14,15].

Another important issue for PICs is the unidirectional transmission of light, which is required for the optical interconnections and optical isolation [16–19]. It is possible to obtain optical isolation by violating the reciprocity condition. In order to design non-reciprocal devices, metamaterials, magneto-optical materials, and indirect interband photonic transitions are introduced [17–19]. However, these structures are not compatible with CMOS technology and demand high input power and large integration area. Besides these proposed techniques, unidirectional light transmission can be partially achieved by designing all-dielectric passive photonic devices by only restricting their operation to the certain input modes [20–22]. It is important to note that the linear and time-independent devices do not break the Lorentz condition. Also, an asymmetric light transmission device cannot be considered as an optical isolator since it does not necessarily require an asymmetric scattering matrix [23]. Even though some controversial studies are proposed on this issue, optical diodes, which are not considered as optical isolators, are introduced by limiting their functionality to finite number of input modes [24].

In the proposed study, the application of attractor selection algorithm [25,26] based on artificial neural networks (ANNs) is introduced to design two different compact efficient photonic devices of an optical coupler and an asymmetric light transmitter (ALT). The designed optical coupler provides the strong confinement of incident light propagating in free-space into Si- waveguide. The designed ALT allows transmission of light in one direction but blocks it in the opposite direction. Both optical coupler and ALT devices are numerically designed by using SOI materials. To the best of authors' knowledge, it is the first time to demonstrate the successful utilization of an approach based on ANNs in order to design PIDs.

2. Problem statement and artificial neural networks based photonic device design

In nanophotonic applications, design of PIDs with high performance as well as their high fabrication densities is a challenging task due to the trade-off between those desired properties. Conventional design methods based on analytic knowledge and intuitions are not sufficient to find a possible solution to balance that trade-off. In this regard, a demand of an

approach that may balance the mentioned trade-off is aroused for designing efficient and compact PIDs. Hence, in this study, we propose the application of attractor selection algorithm to overcome that problem.

ANNs are a subclass of machine learning techniques, which are proven to be highly capable in characterizing nonlinear relationships from pattern recognition to autonomous vehicle control systems. The deep learning paradigm is getting popular and embraced by all fields in science, which is basically a multi-layer neural network. Although its origin dates back to 1980s, the advances in recent years in storage technology and processing capabilities proved feasibility of neural networks on solving problems. For instance, a deep neural network beat all the human crafter methods in the famous ImageNET image recognition competition in 2012 [27]. Also, a computer beat the human champion of game Go for the first time in 2016 by using neural networks [28]. Recently, the effectiveness of machine learning in designing efficient nanophotonic devices is introduced [11,29].

In this study, we applied attractor selection algorithm, which can be considered as reinforcement learning and is based on neural networks, to design photonic devices. Applications of attractor selection algorithm include optimizing optical network topologies [26,30] and routing of vehicular ad hoc networks [31]. The numerical analyses of the designed photonic devices are performed by using three-dimensional (3D) finite-difference time-domain (FDTD) method [32], which is integrated into attractor selection algorithm. Here, the designed photonic devices are intended to be compatible with SOI technology for possible fabrication process in the future. Thus, Si is selected as the underlying main material for the design process. During a design process, an intended photonic device is considered as a matrix of individual cells where high refractive index Si- scatterers are stated as "+1" and air cells are stated as "-1" in the matrix due to the operation of attractor selection algorithm. The sizes of corresponding individual cells are fixed to be 100 nm × 100 nm where the material refractive indices of Si and air are fixed to $n_{Si} = 3.46$ and $n_{air} = 1.0$, respectively. We should note that the fixed sizes of individual cells are chosen in accordance with the recent fabrication technology based on SOI platforms [9,10]. The applied attractor selector algorithm determines the state of each individual cell whether it will be Si or air. As a result, a photonic device can be expressed as a matrix with defined elements of "plus ones" and "minus ones" only.

In order to design a photonic device, its desired optical characteristics should be determined as an objective function for the attractor selection algorithm. For this reason, we defined distinct objective functions for modelling of an optical coupler and an ALT. The mentioned objective function is actually the error value between the performance of currently designed photonic device during the operation of algorithm and the initially predefined desired performance. The algorithm iteratively updates the state of individual cells in a photonic device to minimize that error value.

In the case of an optical coupler, the attractor selection algorithm managed to increase the transmission efficiency for a predefined operating bandwidth in the telecom wavelengths. We set the objective as finding a suitable photonic structure with maximum coupling efficiency for a selected wavelength interval. Here, the corresponding error value is the summation of differences between the transmission efficiency of instant designed photonic device and predefined target value for all wavelengths of the operating bandwidth. In order to design an optical coupler, the error values can be calculated as follows

$$E_{coupler} = \sum_{i=\lambda_{start}}^{\lambda_{end}} \left(T_{desired} - T_i \right) \tag{1}$$

where, $T_{desired}$ is the user defined broadband target transmission efficiency and T_i is the normalized transmission efficiency for as i^{th} selected wavelength of the operating bandwidth. The limits of bandwidth are denoted by λ_{start} and λ_{end}.

Separately, we applied the attractor selection algorithm to obtain an asymmetric light transmission effect. For this purpose, the algorithm is utilized to increase the transmission efficiency in the direction of forward propagation of light but decrease the transmission efficiency in the direction of backward propagation of light. Thus, in the case of designing an ALT, we defined two objectives for algorithm. The first objective is to maximize the transmission efficiency in the forward direction for the selected design wavelength. The second objective of algorithm is to minimize the transmission efficiency in the backward direction for the same operating wavelength. For this reason, we need to calculate multiple error values such as error value for higher forward transmission efficiency and error value for lower backward transmission efficiency. Since the attractor selection algorithm operates only with a single error value, we use the summation of two error values as a total error value to simultaneously minimize the both calculated error values. We used the following formula for error value to design an ALT

$$E_{ALT} = \left(T_{Fdesired} - T_F\right) + \left(T_B - T_{Bdesired}\right) \tag{2}$$

where, T_F and T_B denote the normalized transmission efficiencies of forward and backward directions at the selected design wavelength, respectively. Also, $T_{Fdesired}$ and $T_{Bdesired}$ denote the user defined target transmission efficiencies for forward and backward directions at a design wavelength, respectively.

The intended designs of photonic devices are schematically represented in Figs. 1(a) and 1(b), respectively, for an optical coupler and an ALT. As can be seen from the schematics, the final designed photonic devices will consist of individual Si- cells and air holes that are distributed on SiO$_2$ substrate. In Fig. 1(a) we attempted to depict the compression of incident light (wide yellow arrow in air) into Si- nano-waveguide (narrow yellow arrow). Besides, in Fig. 1(b), the green arrow shows the enabled forward propagation of light, whereas the red curved arrow represents the back reflection of blocked light. Here, the designed intermediate region should provide an asymmetric light transmission effect.
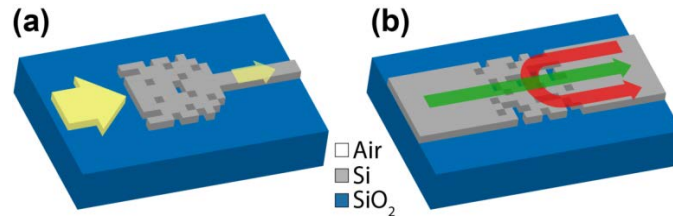

Fig. 1. Schematic representations of the intended design of (a) an optical coupler and (b) an ALT.

At this point, it is important to give detailed explanation for the principle of operation of applied attractor selection mechanism. Since the attractor selection mechanism is a bio-inspired model, it would be beneficial to further explain its biological counterparts. In biological systems, the cell growth is controlled by the interaction of the metabolic reaction network and gene regulatory network in the cell [25]. The gene reaction network produces the proteins that react with the nutrition in the environment. Each gene has an expression level controlling the level of the protein production. In the metabolic reaction network, these proteins convert the nutrition to the substances that are necessary for the cell growth. The amount of the produced substances controls the activity level of the gene regulatory network as a feedback mechanism. A high level of substances implies a favorable condition, so the cell accepts it as an attractor state and continues to run the gene reaction network with the similar expression levels. Otherwise, it means that the current expression levels are not favorable for the current environment, so the expression levels start to deviate from the last attractor as the noise becomes dominant.

During the design process, the photonic device can be interpreted as the level of the protein production, whose expression levels are represented as $x = (x_1, x_2, …, x_n)$. Here, the expression level of x^i, which is between [-1, 1], determines whether the ith individual cell in the photonic device is Si or air. If $x_i < 0$, then i^{th} individual cell in the photonic device is defined to be an air. Otherwise, it is defined to be a Si- individual cell. According to Ref. 26, analytical expression for calculation of x^i is as follows:

$$\frac{dx_i}{dt} = \alpha \cdot \left(f \cdot \left(\sum_j W_{ij} \cdot x_j - \theta \right) - x_i \right) + \eta \tag{3}$$

In Eq. (3), α is the growth rate, which is a function of the error value of the photonic device showing whether the current photonic device is favorable in the current environment. The η is the Gaussian noise term showing the strength of stochastic behavior. The noise dominates the system in case the error value of the photonic device is low and the system changes randomly to find a new attractor state. The deterministic behavior is controlled by the sigmoidal regulation function

$$f(z) = \tan h(\mu z) \tag{4}$$

where, μ is the gain parameter. W is the regulatory matrix, which moves the photonic device to an attractor state when the growth rate is high. θ is the threshold value for expression level. The error value E is then converted to the growth rate α by

$$\alpha = \frac{1}{1 + e^{(\delta \cdot (E - \zeta))}} \tag{5}$$

where δ is the gradient and the ζ is the threshold error rate. The regulatory matrix W is a Hopfield neural network [33] containing a set of possible attractors calculated by using orthogonal projection [34,35]. Let X be a matrix whose rows are the attractors coded according to bipolar coding. First, we calculate the pseudo-inverse matrix X^+. Then the regulatory matrix is calculated by simply

$$W = X^+ X \tag{6}$$

The attractor selection algorithm parameters were empirically set to $\mu = 10$ and $\delta = 0.20$. During the design process of an optical coupler, the threshold error rate is selected as $\zeta = 5$, whereas the threshold error rate is fixed to $\zeta = 1$ in order to design an ALT. The variance of the noise η is selected 0.30. The iterative attractor selection algorithm can be summarized in three phases. Firstly, FDTD method is performed to calculate the error value of the current photonic device. Then, using the growth rate α calculated by the error value and the noise level, the new expression levels $x = (x_1, x_2, …, x_n)$ are calculated. Finally, the individual cells of photonic device are updated according to the new expression levels. It should be noted that the algorithm is manually terminated when the calculated error value does not change for a relatively long time. We want to note that the simulation time for the design of each proposed devices took two months. The computational experiments are done by running three computers in parallel fashion to speed-up the numerical calculations. The hardware specifications of the corresponding computers are as follows: *Computer 1* (3.3GHz Intel i7-3960x CPU, 6 Cores, 32GB RAM); *Computer 2* (2.9GHz Intel Xeon E5-2690 CPUx2, 2x8 Cores, 64 GB RAM); *Computer 3* (2.26GHz Intel Xeon X7560 CPUx2, 2x8 Cores, 512 GB RAM).

3. Results and discussion

In this study, we designed a compact optical coupler with a footprint of 4×2 μm^2 by using attractor selection algorithm. The designed optical coupler consists of Si- individual cells with a size of 100 nm $\times$ 100 nm and a thickness of 240 nm where the Si- nano-waveguide with a

width of 400 nm is butt-coupled to the optical coupling region. Due to goal of obtaining compact coupler, we fix the length of the coupler as 2 µm. In Fig. 2(a), 3D view and top view of the photonic device are depicted with its structural dimensions. We should note that the designed optical coupler confines in-plane incident light injected from free-space into Si-nano-waveguide. The direction of light propagation is denoted by yellow arrow as an inset in Fig. 2(a). Throughout the 3D FDTD simulations, SiO_2 material is selected as a substrate for the optical coupler to ensure the possible realization of SOI platform. The proposed optical coupler is designed to be symmetrical with respect to the x-axis (corresponding axes are shown as inset in Fig. 2(a)). In 3D FDTD simulations to calculate the coupling efficiency of the optical coupler, a broadband plane-wave light source of transverse-electric (TE) polarization covering 1300 nm – 1800 nm range is used to excite the photonic device where the electric field components are along the xy-plane (E_x, E_y) and the magnetic field H_z is perpendicular to the xy-plane. Also, perfectly matched layers are employed in the computational domain to eliminate the undesired back reflections [36].
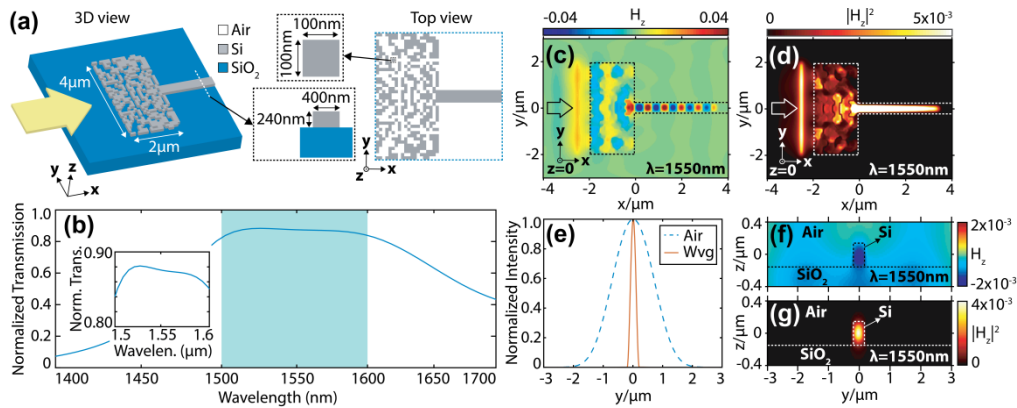

Fig. 2. (a) 3D and top view of designed optical coupler are shown with structural dimensions where the yellow arrow represents the incident light. (b) Normalized transmission efficiency is plotted and shaded region indicates the operating bandwidth of proposed photonic device. (c) Steady state magnetic field and (d) intensity distributions at $z = 0$ plane of 3D FDTD region are given for wavelength of $\lambda = 1550$ nm. Dashed lines indicate the boundaries of optical coupler and direction of incident light is represented by arrows. (e) Lateral cross-sectional intensity profiles at input region (Air) and nano-waveguide region (Wvg) of the device are represented. (f) Field and (g) intensity distributions in yz-plane at nano-waveguide region of the photonic device are given for wavelength of $\lambda = 1550$ nm where dashed lines denote the boundaries of dielectric materials.

As aforementioned, the attractor selection algorithm is applied to design an optical coupler that operates for a defined operating region of telecom wavelengths. In this regard, in Fig. 2(b), we provided the coupling efficiency plot for the final generated optical coupler. In this figure, the shaded region indicates the predefined operating regime of wavelengths between 1500 nm and 1600 nm for design process where they correspond to the λ_{start} and λ_{end} in Eq. (1), respectively. As a result, attractor selection algorithm designed an optical coupler that exhibits the coupling efficiency higher than 84% for a bandwidth of 6.45% centered at the wavelength of 1550 nm as can be seen in Fig. 2(b). At the center wavelength of 1550 nm the corresponding transmission efficiency is calculated as 87.5%. Cross-sectional views of steady state spatial magnetic field H_z and intensity $|H_z|^2$ distributions at $z = 0$ plane of 3D FDTD region are represented in Fig. 2(c) and (d), respectively, for the incident wavelength of $\lambda = 1550$ nm. In these figures, the dashed lines indicate the boundaries of the proposed optical coupler. As can be seen from Fig. 2(c), the designed photonic device couples incident light into a nano-waveguide. It should also be pointed out that the proposed optical coupler has a high conversion ratio of 10:1, i.e., the spatial width of the coupling region is 4 µm, whereas

the Si- nano-waveguide has the spatial width of 0.40 µm. As can be seen from Figs. 2(c) and 2(d), the designed coupling region minimizes the back reflections originated from the interface between air and coupling region and squeezes down the injected light from free-space into output nano-waveguide with a high coupling efficiency of 87.5%. The compression of the propagating wave is achieved by transforming the incident plane wavefronts to the converging wavefronts, i.e., propagating light converges into the point at the interface between coupler and nano-waveguide junction region. Therefore, converged light that revealed at the entrance of the butt-coupled nano-waveguide is easily confined and allowed to propagate with high transmission efficiency. In Fig. 2(e), the cross-sectional intensity profiles along y-axis at the input (air) and the output (on nano-waveguide) of the designed device is superimposed to show the spatial compression of incident light. In Figs. 2(f) and 2(g), the cross-sections of steady state magnetic field and intensity distributions at *yz*-plane on the nano-waveguide are shown, respectively, where the boundaries of the device are denoted with the dashed lines. It can be seen from these figures that the coupled light is strongly confined in the nano-waveguide with negligible leakage to the SiO$_2$ substrate.
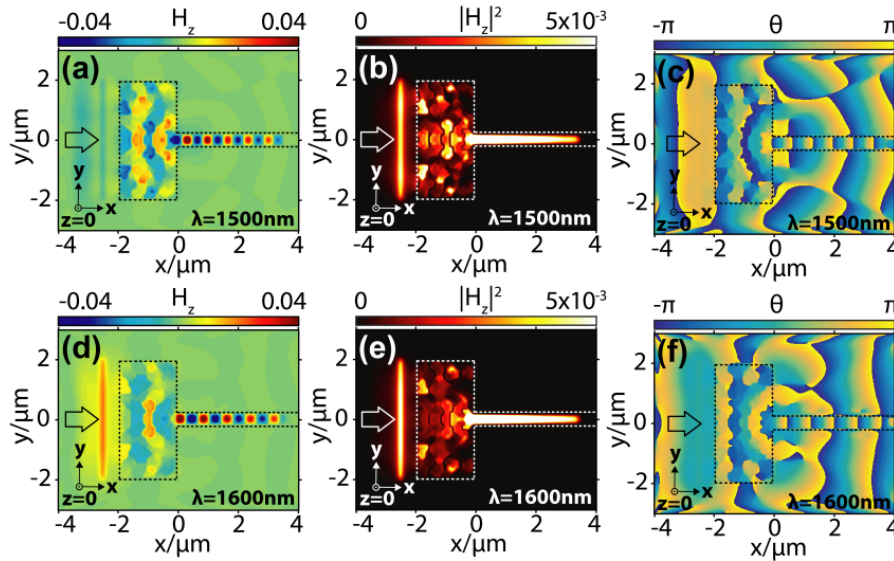

Fig. 3. (a) Field, (b) intensity and (c) phase distributions at *z* = 0 plane of 3D FDTD region are given for wavelength of *λ* = 1500 nm. (d) Field, (e) intensity and (f) phase distributions at *z* = 0 plane of FDTD region are given for wavelength of *λ* = 1600 nm. Dashed lines represent the boundaries of optical coupler and arrows indicate the direction of incident light.

In order to investigate the broadband operation of designed optical coupler, steady state magnetic field, intensity and phase distributions at *z* = 0 cross-sectional plane of 3D FDTD region are calculated and represented in Figs. 3(a)-3(c) for wavelength of 1500 nm and in Figs. 3(d)-3(f) for wavelength of 1600 nm. These selected wavelengths are the edge wavelengths of selected operating bandwidth. According to the transmission efficiency plot given in Fig. 2(b), the coupling efficiencies of designed optical coupler at 1500 nm and 1600 nm are equal to 84% and 85%, respectively. In this regard, the propagating field distributions shown in Fig. 3(a) and 3(d) indicate the strong coupling effect. Moreover, as seen from Fig. 2(b), the coupling efficiency plot is nearly linear (negligible fluctuations) within the defined operating bandwidth. Therefore, one can expect the strong light confinement effect for the intermediate operating wavelengths that lie between wavelengths of 1500 nm and 1600 nm. Similarly, for the same operating edge wavelengths, one can see the strong light confinement in nano-waveguide from spatial intensity distributions, which are given in Figs. 3(b) and 3(e). In addition, we extracted and plotted the related phase distribution for the wavelength of 1500

nm and 1600 nm in Figs. 3(c) and 3(f), respectively. The phase distributions show that the incident light with plane phase fronts transformed to the convex shaped phase fronts inside the optical coupler. As a result, the propagating light with the converged phase fronts is confined into the nano-waveguide. It is important to note that the dashed lines indicate the boundaries of coupling region and butt-coupled nano-waveguide in Figs. 3(a)-3(f).
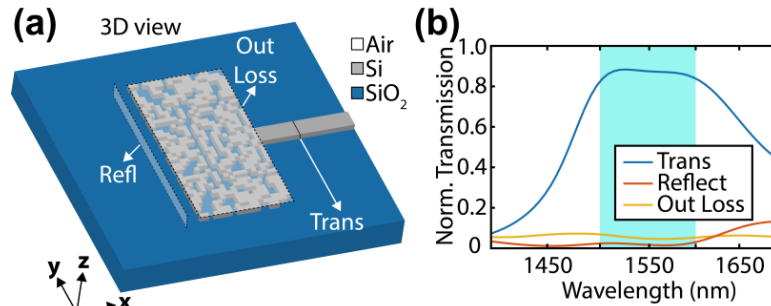

Fig. 4. (a) Locations of monitors in order to calculate transmission, reflection and out-of-plane loss are shown on 3D view of designed optical coupler. (b) Transmission, reflection and out-of-plane loss efficiencies are plotted where shaded region indicates the operating bandwidth.

Further, we analyze the reflection and out-of-plane loss characteristics of the designed optical coupler. For this reason, we placed an optical power monitor behind the incident light source to calculate reflection from the entrance surface of the designed photonic device. In addition, we placed an optical power monitor above the coupling region to calculate the out-off-plane losses. In Fig. 4(a), locations of corresponding monitors are schematically illustrated as perspective 3D view. The calculated efficiencies are plotted in Fig. 4(b). As can be seen, the reflected optical power is under 2.5% of total input optical power and out-off-plane loss is calculated as less than 5% at the operating bandwidth. The designed optical coupler has been examined not only in terms of the transmission efficiency but also in terms of the magnetic field dynamics and we demonstrate the successful application of attractor selection mechanism based on artificial neural networks. Also, one can consider other coupling scenarios such as fiber to waveguide coupler, waveguide to waveguide and free space to waveguide. Such approaches can be targeted with the algorithm developed in the present work. We should note that there are various problems in the integrated photonics that need to be improved to obtain efficient, compact and broadband manipulation of photons.

In addition to the coupler design, here we considered the design of an ALT device via the attractor selection algorithm. The proposed photonic device has compact footprint size of $2 \times 2 \ \mu m^2$ with a thickness of 300 nm. Similarly, in the design of optical coupler device, Si-individual cells with dimensions of 100 nm $\times$ 100 nm are intelligently distributed on a SiO_2 substrate to generate an ALT by the attractor selection algorithm. In 3D FDTD simulations of the ALT design, TE polarized plane-wave source is employed and the design wavelength is fixed to 1550 nm. The asymmetric light transmission region (designed region) is sandwiched between input and output Si- waveguides with the spatial widths of 2 μm and thicknesses of 300 nm as can be seen in Fig. 5(a). Also, in Fig. 5(b), the top view of the designed photonic device is schematically represented where forward and backward directions are indicated by blue and red arrows, respectively. As expressed in Eq. (2) the purpose of implemented attractor selection algorithm is to allow forward light transmission and block backward light propagation within the ALT device. It should be noted that, during the design process, incident light is coupled to the input waveguide and transmission efficiency is calculated in the output waveguide. Another important point to be raised is that the definitions of the terms of "input" and "output" are depends on the direction of excitation of the designed ALT where "input" corresponds to the location of the light source and "output" defines the location of optical power monitor. The placed monitors inside the input and output waveguides are

shown in the 3D view of designed ALT in Fig. 5(c). We should note that only the transmission efficiencies in both directions are considered during the design process. Moreover, reflection and out-off-plane loss characteristics of the designed ALT are also investigated and the locations of the required optical power monitors are also depicted in Fig. 5(c). Corresponding transmission, reflection and out-of-plane loss efficiencies are plotted in Fig. 5(d) for both forward and backward directions where the design wavelength of 1550 nm is indicated. For the forward direction, transmission efficiency of incident light (T_F) is calculated as 88.1% by using whereas the backward transmission efficiency (T_B) is suppressed to be 8.6% at the design wavelength. The designed ALT has an operating bandwidth of 3.47% (the bandwidth is shown by shaded region in Fig. 5(d)), i.e., between the wavelengths of 1527 nm and 1581 nm, where the forward transmission efficiency is higher than 80% and backward transmission is lower than 10%. Here, forward reflection efficiency (R_F) and backward reflection efficiency (R_B) are calculated as 1.7% and 58%, respectively, which is expected for an ALT. In addition, out-of-plane losses are calculated as 4.1% and 5.9% for forward and backward directions, respectively. It can be concluded that the design region does not allow the incident light escaping to the outer-plane. However, especially for backward direction, large amount of energy may leave the device from its sides and leak to the substrate.
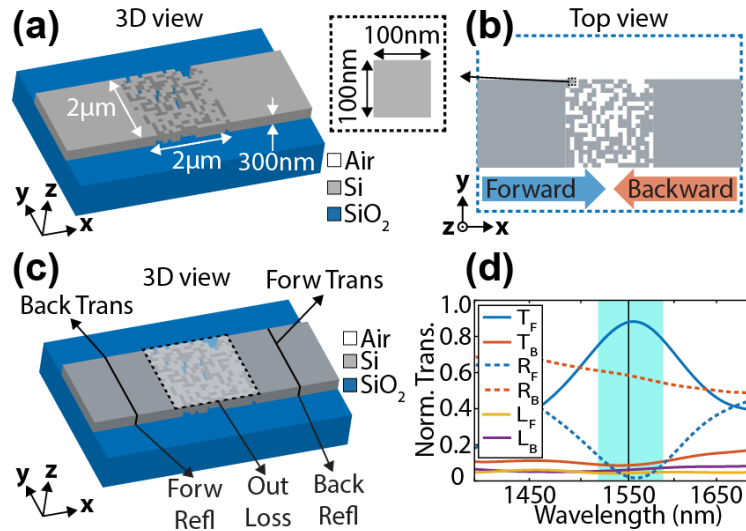

Fig. 5. (a) 3D view and (b) top view of the designed ALT are represented with structural dimensions. Forward and backward directions of incident light are indicated with blue and red arrows, respectively. (c) Positions of optical power monitors in order to calculate transmission, reflection and out-of-plane loss for both forward and backward directions are schematically represented on 3D view of designed ALT. (d) Normalized efficiencies for forward transmission (TF), backward transmission (TB), forward reflection (RF), backward reflection (RB), forward out-of-plane loss (LF) and backward out-of-plane loss (LB) are plotted where yellow line indicates the operating wavelength of λ = 1550 nm. The bandwidth is shown by shaded region in Fig. 5(d)).

In addition, we investigated the cross-sectional steady state magnetic fields and intensities of the designed asymmetric light transmitter operating for both forward and backward directions at wavelength of 1550 nm. In Figs. 6(a) and 6(b), cross-sectional views at $z = 0$ plane in 3D FDTD computation domain for magnetic field and intensity distributions of forward direction are given, respectively. Also, in Figs. 6(c) and 6(d), cross-sectional views of magnetic field and intensity distributions at the yz-plane ($x = 2$ μm location) on output waveguide for forward direction are given, respectively. Similarly, cross-sectional views of magnetic field and intensity distributions for backward excitation case are extracted at $z = 0$

plane which are represented in Figs. 6(e) and 6(f), respectively. The cross-sectional views of magnetic field and intensity distributions at *yz*-plane (*x* = −2 µm location) on output waveguide for backward direction are shown in Figs. 6(g) and 6(h), respectively. In these figures, dashed lines denote the boundaries of design region and waveguides. Also, forward and backward directions of incident light are denoted by arrows left-to-right and right-to-left, respectively. As can be seen from the Figs. 6(a) and 6(e), the coupled light at output waveguides displays multi-mode characteristic even if the incident coupled light has single-mode characteristic at the input waveguides. Also, this effect can be clearly observed from cross-sectional views of confined magnetic fields in Figs. 6(c) and 6(g), the transmitted light exhibits multi-mode characteristic in output waveguides for both forward and backward directions. One can conclude that the arising mode order conversion effect is the main physical mechanism of asymmetric transmission of light. In other words, the intelligently disordered modulation of refractive index introduces a distortion for input single-mode, which results in a multi-mode guided light at output waveguide. Thus, the propagation of light is enabled in the forward direction but almost disabled in the backward direction since the observed multi-mode in the backward direction is not supported by the design medium. While forward propagation of light is allowed through the designed medium, due to highly scattering nature of the refractive index profile, phase distortion, and multi-mode generation occur. However, in the reverse direction, strong back-reflection of light gives rise to almost no light penetration to the other side.
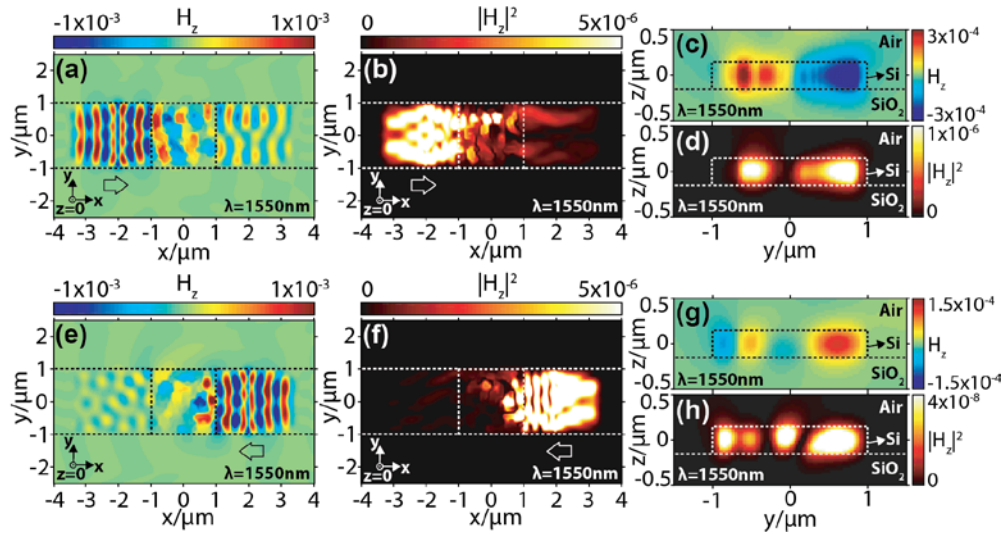

Fig. 6. For forward direction, (a) magnetic field and (b) intensity distributions at z = 0 plane at wavelength of λ = 1550 nm. Cross-sectional views of (c) magnetic field and (d) intensity distributions in yz-plane (x = 2 µm location) are shown for forward direction. For backward direction, (e) magnetic field and (f) intensity distributions at z = 0 plane. Cross-sectional views of (g) magnetic field and (h) intensity distributions in yz-plane (x = −2 µm location) are shown for backward direction. The dashed lines represent the boundaries of design medium and waveguides. The arrows indicate the forward (left-to-right) and backward (right-to-left) directions of incident light.

The proper optical isolation is the perfect prevention of light propagation in backward direction for any order of coupled modes and can only be achieved by breaking the Lorentz symmetry condition [23]. Selection of different guided-modes at input and output for unidirectional light transmission is not sufficient to obtain optical isolation. However, if we restrict the operation of our designed photonic device to certain guided-modes, we can consider it as a kind of optical diode. It should be noted that the proposed ALT does not function as an optical isolator. In order to fully examine the optical isolation effect, all

possible guided modes for backward direction should be investigated. Because the total energy is irregularly divided on different modes, some selected modes can exhibit unidirectional light transmission characteristic. In other words, one particular mode can have low backward transmission efficiency whereas another mode can have relatively high backward transmission efficiency. If one selects the particular guided-mode with low backward transmission efficiency, it cannot be considered as an optical isolation since "*an asymmetric scattering matrix*" is required for all possible guided modes to obtain optical isolation. Furthermore, if one chooses linear and time-independent materials to design a photonic device, it will have a symmetric scattering matrix and thus, it will be impossible to achieve an optical isolation. In the light of these given explanations, we can conclude that our proposed ALT device is not an optical isolator because the photonic device is designed made of all-dielectric materials. On the other hand, designed compact photonic device exhibits asymmetric light transmission behavior due to the difference between the mode orders of oppositely propagating waves.

In addition, we performed FDTD simulations to present the robustness of the proposed optical coupler and ALT devices for possible fabrication imperfections. For this purpose, we introduced random noise of 5%, i.e., random modulation, to 2D-code-like structures in order to simulate the possible fabrication errors of missing air and Si- cells. At the wavelength of 1550 nm, the original device has transmission efficiency of 87.5% whereas the imperfect device shows a transmission efficiency of %83.2. Hence, one can consider that the difference between calculated transmission efficiencies of original and imperfect is at a reasonable level. Similarly, we introduce a random noise of 5% to the designed ALT device to analyze its performance variation due to fabrication imperfections of missing Air/Si- cells. The proposed original ALT device has the transmission efficiencies of 88.1% and 8.6%, respectively, for forward and backward excitation at wavelength of 1550 nm. On the other hand, the forward and backward transmission efficiencies are calculated as 81.4% and 13.8%, respectively, for imperfect ALT device operating at 1550 nm. Moreover, we considered additional fabrication error which can appear due to variations in cell spatial sizes. Hence, we randomly varied the cell sizes of proposed coupling and ALT devices between 95 nm and 105 nm. Here, the transmission efficiency of coupling device was decreased to 80.6% at the operating wavelength of 1550 nm. Furthermore, the forward transmission efficiency of imperfect ALT device is calculated as 78.9% whereas its backward transmission efficiency is equal to 12.2%. As a result, the designed devices can be considered as robust to the small imperfections in cell sizes.

4. Conclusion

In summary, we propose a new design approach in nanophotonics, which is based on attractor selection algorithm and demonstrate its applications by designing an optical coupler and an ALT. The performed 3D FDTD analyses show that the designed photonic integrated devices have compact sizes, high efficiencies, and compatibility with CMOS fabrication technology. The proposed optical coupler with footprint of 4×2 μm^2 has the coupling efficiency of 87.5% and conversion ratio of 10:1 at optical telecom wavelength of 1550 nm. Also, it has broad operating bandwidth of 6.45% for coupling efficiency over 80%. The proposed ALT exhibits unidirectional light transmission characteristic for certain guided-modes with forward transmission efficiency of 88.1% and backward transmission efficiency of 8.6% at wavelength of 1550 nm. The bandwidth of 3.47% is calculated for the designed ALT where the forward transmission efficiency is higher than 80% and backward transmission efficiency is under 10%. The designed ALT has footprint of only 2×2 μm^2 which is the smallest all-dielectric ALT reported to date. In addition, designed photonic devices are feasible for possible fabrication process. To conclude, attractor selection algorithm based on ANNs can be considered as a powerful design tool for the future of photonic integrated devices.

References

1. R. Nagarajan, C. H. Joyner, R. P. Schneider, Jr., J. S. Bostak, T. Butrie, A. G. Dentai, V. G. Dominic, P. W. Evans, M. Kato, M. Kauffman, D. J. H. Lambert, S. K. Mathis, A. Mathur, R. H. Miles, M. L. Mitchell, M. J. Missey, S. Murthy, A. C. Nilsson, F. H. Peters, S. C. Pennypacker, J. L. Pleumeekers, R. A. Salvatore, R. K. Schlenker, R. B. Taylor, H. Tsai, M. F. Van Leeuwen, J. Webjorn, M. Ziari, D. Perkins, J. Singh, S. G. Grubb, M. S. Reffle, D. G. Mehuys, F. A. Kish, and D. F. Welch, "Large-scale photonic integrated circuits," IEEE J. Sel. Top. Quantum Electron. **11**(1), 50–65 (2005).
2. L. A. Coldren, S. W. Corzine, and M. L. Mashanovitch, *Diode Lasers and Photonic Integrated Circuits*, (Wiley, 2012).
3. V. R. Almeida, C. A. Barrios, R. R. Panepucci, and M. Lipson, "All-optical control of light on a silicon chip," Nature **431**(7012), 1081–1084 (2004).
4. G. T. Reed, G. Mashanovic, F. Y. Gardes, and D. J. Thomson, "Silicon optical modulators," Nat. Photonics **4**(8), 518–526 (2010).
5. D. Liang and J. E. Bowers, "Recent progress in lasers on silicon," Nat. Photonics **4**(8), 511–517 (2010).
6. J. Lu and J. Vučković, "Nanophotonic computational design," Opt. Express **21**(11), 13351–13367 (2013).
7. A. Y. Piggott, J. Lu, K. G. Lagoudakis, J. Petykiewicz, T. M. Babinec, and J. Vuckovic, "Inverse design and demonstration of a compact and broadband on-chip wavelength demultiplexer," Nat. Photonics **9**(6), 374–377 (2015).
8. L. Su, A. Y. Piggott, N. V. Sapra, J. Petykiewicz, and J. Vuckovic, "Inverse design and demonstration of a compact on-chip narrowband three-channel wavelength demultiplexer," ACS Photonics **5**(2), 301–305 (2018).
9. B. Shen, P. Wang, R. Polson, and R. Menon, "An integrated-nanophotonics polarization beamsplitter with 2.4 × 2.4 μm² footprint," Nat. Photonics **9**(6), 378–382 (2015).
10. B. Shen, R. Polson, and R. Menon, "Integrated digital metamaterials enables ultra-compact optical diodes," Opt. Express **23**(8), 10847–10855 (2015).
11. M. Turduev, E. Bor, C. Latifoglu, I. H. Giden, Y. S. Hanay, and H. Kurt, "Ultra-compact photonic structure design for strong light confinement and coupling into nano-waveguide," J. Lightwave Technol. **36**(14), 2812–2819 (2018).
12. D. Liu, Y. Tan, E. Khoram, and Z. Yu, "Training deep neural networks for the inverse design of nanophotonic structures," ACS Photonics **5**(4), 1365–1369 (2018).
13. S. Molesky, Z. Lin, A. Y. Piggott, W. Jin, J. Vuckovic, and A. W. Rodriguez, "Outlook for inverse design in nanophotonics," https://arxiv.org/abs/1801.06715.
14. A. Y. Piggott, J. Lu, T. M. Babinec, K. G. Lagoudakis, J. Petykiewicz, and J. Vučković, "Inverse design and implementation of a wavelength demultiplexing grating coupler," Sci. Rep. **4**(1), 7210 (2014).
15. B. Shen, P. Wang, R. Polson, and R. Menon, "Integrated metamaterials for efficient and compact free-space-to-waveguide coupling," Opt. Express **22**(22), 27175–27182 (2014).
16. A. Cicek, M. B. Yucel, O. A. Kaya, and B. Ulug, "Refraction-based photonic crystal diode," Opt. Lett. **37**(14), 2937–2939 (2012).
17. L. Bi, J. Hu, P. Jiang, D. H. Kim, G. F. Dionne, L. C. Kimerling, and C. A. Ross, "On-chip optical isolation in monolithically integrated non-reciprocal optical resonators," Nat. Photonics **5**(12), 758–762 (2011).
18. M. Mutlu, A. E. Akosman, A. E. Serebryannikov, and E. Ozbay, "Diodelike asymmetric transmission of linearly polarized waves using magnetoelectric coupling and electromagnetic wave tunneling," Phys. Rev. Lett. **108**(21), 213905 (2012).
19. Z. Yu and S. Fan, "Complete optical isolation created by indirect interband photonic transitions," Nat. Photonics **3**(2), 91–94 (2009).
20. V. Liu, D. A. B. Miller, and S. Fan, "Ultra-compact photonic crystal waveguide spatial mode converter and its connection to the optical diode effect," Opt. Express **20**(27), 28388–28397 (2012).
21. C. Wang, C. Z. Zhou, and Z. Y. Li, "On-chip optical diode based on silicon photonic crystal heterojunctions," Opt. Express **19**(27), 26948–26955 (2011).
22. C. Wang, X. L. Zhong, and Z. Y. Li, "Linear and passive silicon optical isolator," Sci. Rep. **2**(1), 674 (2012).
23. D. Jalas, A. Petrov, M. Eich, W. Freude, S. Fan, Z. Yu, R. Baets, M. Popovic, A. Melloni, J. D. Joannopoulos, M. Vanwolleghem, C. R. Doerr, and H. Renner, "What is- and what is not- an optical isolator," Nat. Photonics **7**(8), 579–582 (2013).
24. F. Callewaert, S. Butun, Z. Li, and K. Aydin, "Inverse design of an ultra-compact broadband optical diode based on asymmetric spatial mode conversion," Sci. Rep. **6**(1), 32577 (2016).

25. A. Kashiwagi, I. Urabe, K. Kaneko, and T. Yomo, "Adaptive response of a gene network to environmental changes by fitness-induced attractor selection," PLoS One **1**(1), e49 (2006).
26. Y. Koizumi, T. Miyamura, S. Arakawa, E. Oki, K. Shiomoto, and M. Murata, "Adaptive virtual network topology control based on attractor selection," J. Lightwave Technol. **28**(11), 1720–1731 (2010).
27. A. Krizhevsky, I. Sutskever, and G. F. Hinton, "Imagenet classification with deep convolutional neural networks," in *Adv. Neural Inf. Process. Syst.* (2012), pp. 1097–1105.
28. D. Silver, A. Huang, C. J. Maddison, A. Guez, L. Sifre, G. van den Driessche, J. Schrittwieser, I. Antonoglou, V. Panneershelvam, M. Lanctot, S. Dieleman, D. Grewe, J. Nham, N. Kalchbrenner, I. Sutskever, T. Lillicrap, M. Leach, K. Kavukcuoglu, T. Graepel, and D. Hassabis, "Mastering the game of Go with deep neural networks and tree search," Nature **529**(7587), 484–489 (2016).
29. I. Malkiel, A. Nagler, M. Mrejen, U. Arieli, L. Wolf, and H. Suchowski, "Deep learning for design and retrieval of nano-photonic structures," https://arxiv.org/abs/1702.07949.
30. Y. S. Hanay, S. Arakawa, and M. Murata, "Network topology selection with multistate neural memories," Expert Syst. Appl. **42**(6), 3219–3226 (2015).
31. D. Tian, J. Zhou, Y. Wang, G. Zhang, and H. Xia, "An adaptive vehicular epidemic routing method based on attractor selection model," Ad Hoc Netw. **36**(2), 465–481 (2016).
32. A. F. Oskooi, D. Roundy, M. Ibanescu, P. Bermel, J. D. Joannopoulos, and S. G. Johnson, "Meep: a flexible free-software package for electromagnetic simulations by the FDTD method," Comput. Phys. Commun. **181**(3), 687–702 (2010).
33. J. J. Hopfield, "Neural networks and physical systems with emergent collective computational abilities," Proc. Natl. Acad. Sci. U.S.A. **79**(8), 2554–2558 (1982).
34. Y. Baram and A. R. Center, "Orthogonal patterns in binary neural networks," https://ntrs.nasa.gov/archive/nasa/casi.ntrs.nasa.gov/19880008936.pdf.
35. Y. S. Hanay, Y. Koizumi, S. Arakawa, and M. Murata, "Virtual network topology control with Oja and APEX learning," Proc. 24th Int. Teletraffic Congr. **47**, 1–6 (2012).
36. J. A. Berenger, "Perfectly matched layer for the absorption of electromagnetic waves," J. Comput. Phys. **114**(2), 185–200 (1994).